engineering proceedings

MDPI

Proceeding Paper

MD Average of Vibrational Spectra of Nucleotides in a SERS Sensor Simulation with Varying Number of Au Nanoparticles †

Tatiana Zolotoukhina * and Kota Maruyama

Department of Mechanical Engineering, University of Toyama, Toyama 930-8555, Japan;
* Correspondence: zolotu@eng.u-toyama.ac.jp; Tel.: +81-76-445-6739
† Presented at the 3rd International Electronic Conference on Biosensors, 8–21 May 2023; Available online: https://iecb2023.sciforum.net.

Abstract: Applying the surface-enhanced Raman scattering (SERS) method to detect bioactive molecules such as DNA, proteins, and drugs has significant potential for structure-sensitive nondestructive chemical analysis. The SERS discrimination of single molecule oligomers in DNA, microRNA, and proteins has attracted wide attention due to the possibility of developing new sensing technology. The collected signal's sensitivity has the level of detection of single oligomers, which can be compared with the simulation results corresponding to the sensor structure. We investigate the averaging method of the individual bond spectra for DNA nucleotides in the ring part of the pyrimidine (6-ring) and purine (6–5-ring) bases to form vibrational spectra obtained by molecular dynamics (MD) simulation. The system consists of the Au nanoparticles (from 1 to 4 NP assay) attached to a graphene sheet at the edge of the nanopore that localizes in the nanopore nucleotide interaction & spectral enhancement. The nucleotide translocation velocity set at 0.025 m/s compares with the experimental range. The vibrational spectra ring average has been tested for adenine and guanine with close correspondence (in the 500–1700 cm^{-1} range) to the experimental Raman & SERS spectra and extended to cytosine and thymine nucleotides. We also modified the number of the Au nanoparticles from 1 NP to 4 identical NPs to evaluate the influence of the interaction on the MD transient spectra. The variations of mode frequencies and amplitudes due to the number of Au NPs in bond spectra, as well as ring averages, mark the corresponding Au–nucleotide interactions and are considered to be used as training sets for machine learning methods.

Keywords: vibrational spectra; molecular dynamics; nucleotides; Au nanoparticle; SERS;

Citation: Zolotoukhina, T.; Maruyama, K. MD Average of Vibrational Spectra of Nucleotides in a SERS Sensor Simulation with Varying Number of Au Nanoparticles. *Eng. Proc.* **2023**, *35*, x. https://doi.org/10.3390/xxxxx

Academic Editor(s):

Published: 8 May 2023

1. Introduction

Nanophotonic sensing methods based on the SERS detection of DNA, RNA, and protein sequences on solid-state and biological platforms [1,2] have reached single nucleotide or amino acid sensitivity [1–13]; however, a number of challenges still remain ahead of technological implementation. High sensitivity and selectivity in small volumes have been achieved by manipulation of plasmonic enhancers used to create hot spots for the measured molecules by using different shapes, assays, and surfaces of gold or silver nanostructures [12,13]. Some methods based on trapping a gold nanoparticle in a localized space of nanohole [14] have been demonstrated. The use of solid-state plasmonic platforms has the advantage of fine-tuning such sensing systems' physical and chemical properties. However, the time and space resolution of the solid-state platforms still remains the major challenge to oligomer sequencing together with translocation mechanism control. The single-molecule spatial and temporal localization of a nanosized optical hot spot is able to achieve a resolution high enough for single oligomer detection. The principle of the plasmonic nanopore can be applied to enhanced optical spectroscopy for multiplexed DNA and protein sequencing [15]. Each oligomer has its own Raman fingerprint, and discrimination among them has been proven by the use of SERS [16,17]. In addition

to distinguishing oligomer molecules in sequencing [18,19], the SERS spectrum could provide additional information on molecular states, including oxidation and methylation [20,21].

For high spatial resolution, nano-objects inside a nanopore for single-molecule SERS measurements must be precisely localized. The duration of the interaction between the oligomer and enhancer should be large enough to ensure a high signal-to-noise ratio in single DNA/protein analysis to acquire a sufficient number of spectra for averages. Typical translocation of a DNA base or an amino acid residual through solid-state nanopores takes nano- to microseconds, while typical acquisition time takes a millisecond per frame in SERS spectra [22]. The duration of the acquisition process ensures the spectral average of the rotation and conformation motion. The orientation dependence of spectra was confirmed [23] and showed that the orientation of single Rhodamine 6G and oxygenated/deoxygenated states of single hemoglobin could be observed by SERS.

Protein detection using SERS [24,25] demonstrated the typical behavior of a linked single molecule SERS including spectral fluctuations and blinking. From the above problems, the translocation of measured molecules in a designed nanopore can lead to a better signal in the nanopore for the high-speed acquisition of SERS spectra. The different orientations of single oligomers inside the nanopore provide information on the state and interaction of the biomolecule. Various orientations of molecules usually cause the fluctuation of SERS spectra, causing peak shifts, appearances, disappearances, or intensity changes [25]. Therefore, obtained SERS signals will benefit from decoding contributing states and interactions by machine learning algorithms.

Improvement in spatial resolution can be achieved when the sensor can be confined down to the atomic thickness of the 2D material. The atomic thickness also leads to control of nanopore translocation time and possible changes in molecule orientation to identify oligomers. SERS plasmonic nanoparticles were integrated with a nanopore in a 2D material's membrane, especially graphene [26–32] and hexagonal BN [33–36]. The detection of DNA/RNA oligomers, mononucleotides [37–39], and nucleobases [40] with SERS techniques has been demonstrated.

Simulation of the SERS sensors with a configuration close to the experimental one is required to attribute orientation and conformation-dependent spectra of DNA/protein oligomers at the time of relative motion inside the sensing system. The ab initio MD method reproduces high-fidelity orientation-dependent infrared and Raman spectra but remains computationally extensive [41]. The molecular dynamics (MD) method can simulate vibrational spectra over a correlation time span as already time-averaged; however, each bond spectra is estimated individually that ensure orientation and conformation resolved sensing. In our system, the 2D graphene nanopore is combined with a pyramidal Au nanoparticle (NP) (single vs. four identical pyramids) attached at the edge of the nanopore to form the SERS sensor. Such design allows guiding the single oligomer through the created "hot" spot [42–44]. Individual bond spectra should be averaged to include contributions of multiple bonds into oligomer spectrum. We study the vibrational spectra of the four DNA nucleotides together with the methylated forms of cytosine and adenine in the dynamic interaction with the Au NP attached to the graphene nanopore. For bonds in each nucleobase, averages for two types of nucleotides, purine and pyrimidine, were considered over bonds in the two-carbon nitrogen ring (adenine and guanine) and one-carbon nitrogen ring (thymine and cytosine) in the clockwise direction to include each ring bond. The frequencies and modes that can serve as markers of the corresponding nucleotides and their methylated forms are estimated and compared with existing experimental Raman and SERS spectra. The way to input obtained by MD nucleotide's vibrational spectra into machine learning (ML) random forest algorithm as training sets for spectral recognition is discussed.

2. Model and Methods

The present study uses MD simulation of the system consisting of the following components: nucleotide, Au NP (1 to 4 Au_{20} pyramidal shaped NP), and single layer graphene with nanopore to translocate the nucleotide as seen in Figure 1. With the proven influence of the system components on the vibrational spectra of each part [43,44], the way to collect spectra of individual bonds into the spectra distinguishing each nucleotide and its methylated forms has been tested. The nucleotide vibrational frequencies were attributed to stretching, bending, or ring-breathing modes. The vibrational frequencies of the ring bond were found to incorporate at varying intensity levels (due to atomic velocity vector projections onto all bond axes containing the atom) the spectral modes adjacent to the atom bonds. In the nucleobase, in such a way, ring bond spectra include modes of amino and methyl groups as well as bonded to the ring oxygen and hydrogen. Therefore, correct averages over ring bond spectra are expected to enhance dominant modes and suppress the off-phase numerical noise.

For each atom in the bonds of the oligomer, the vibrational density of states (DOS) is calculated during translocation time through the graphene nanopore with attached Au NPs to accumulate all atomic spectra of the oligomer bonds. The calculation method is described in detail in [43,44]. Because the interaction causes shift and/or intensity changes in selected vibration frequencies of the nucleotide spectra, the starting point and translocation speed were the same for each nucleotide and methylated form studied. The initial nucleotide conditions ensure a similar interaction duration with the sensing system for the measured molecule.

The structure of the SERS sensor in MD calculations with components is presented in Figure 1. To the graphene sheet with the 1.5 nm in diameter pore at its center; the pyramidal Au_{20} NP is attached at the edge of the pore. The initial location of the cytosine nucleotide at the 4 Å distance from the pore edge is selected to maximize the interaction energy with graphene and Au NP without "sticking" to the sensor part of the system. All Van der Waals interactions between the NP, graphene, and the molecule at translocation in the pore are included in the correlation interval by setting the initial oligomer z distance from the pore plane. The graphene sheet is oriented in the x-y-plane, the edges along the y-axis are fixed, and the edges along the x-axis are free. The nucleotide moves with a given added velocity of the center of mass ($v_{c.o.m.}$) in the positive z-direction $v_{COM} = 0.025\, m/s$ that overall reproduces the 0.1–0.01 m/s motion in a constant electric field in the experiments [45,46]. The system atoms, except fixed ones, are thermally relaxed; sampling is done at 300 K for graphene and 30°C for nucleotide, as marked in Figure 1. The attachment distance of Au NPs to the graphene surface is 3 Å [47]. The LJ interaction potential between Au NP and graphene has $\sigma(C - Au) = 2.74$ Å and $\varepsilon(C - Au) = 0.022$ eV and truncated at 4.50 Å [47]. In the production run, COM coordinates of the Au NPs have been kept attached to graphene. The graphene-nucleotide and Au NP- nucleotide potentials are considered VdW ones to avoid bond creation and nucleotide attachment in the pore.

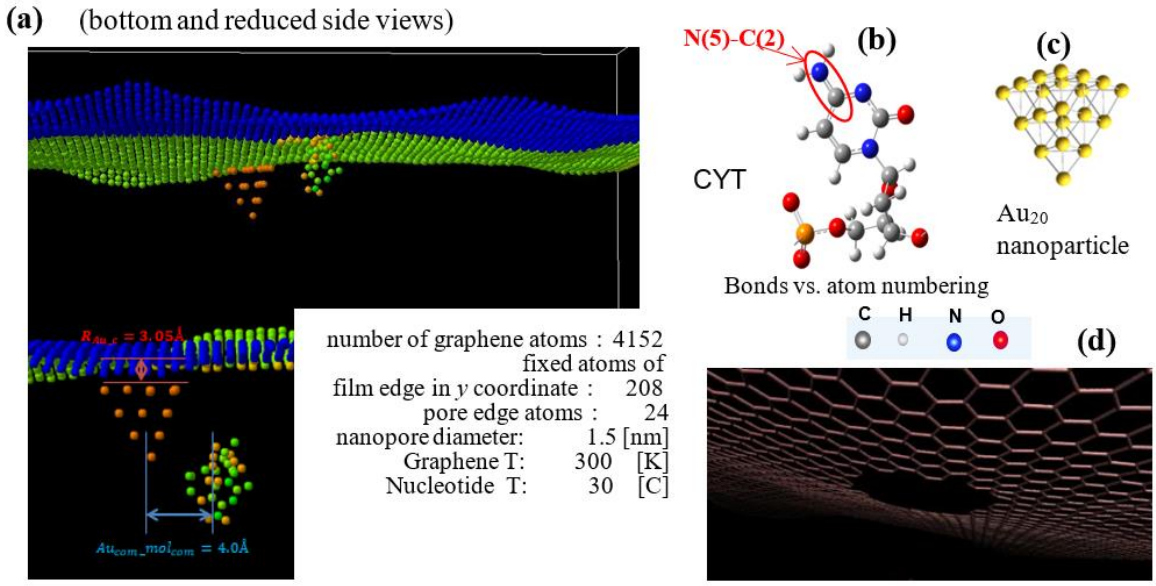

Figure 1. The structure of the SERS sensor in MD calculations (**a**) The initial translocation position of cytosine nucleotide at and inside of the graphene pore. The orientation of the nucleotide's cyclic plane is at 30° to the z-x plane. Atoms are shown: C in grey, N in blue, O in red, and H in light grey. (**b**) Cytosine (right) is shown with an example of corresponding atom numbering for bonds. (**c**) Au_{20} nanoparticle optimized by DFT GGA calculations. (**d**) Nanopore of 1.5 nm diameter with C bonds at its edge in graphene sheet.

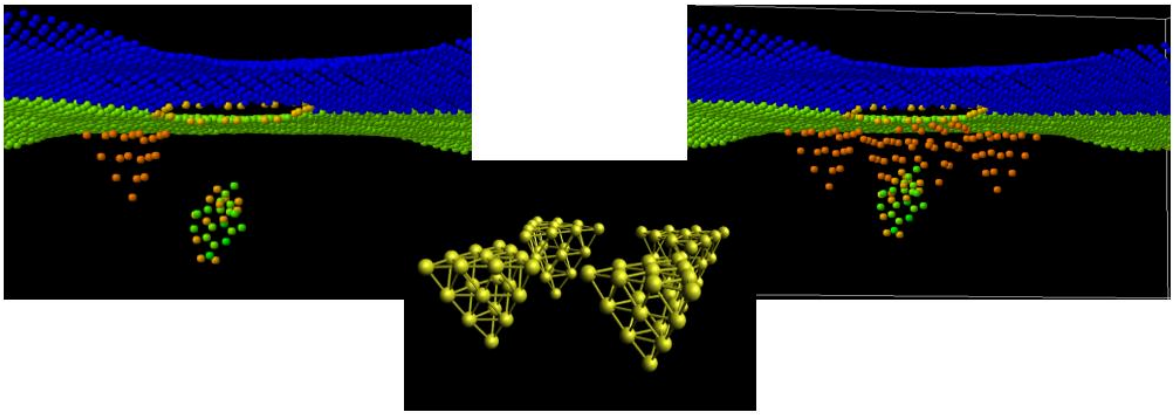

Figure 2. Simulation models with 1 and 4 Au NPs arranged at the edge of graphene nanopore and cytosine oligomer at the start of translocation. At the central panel, 4 Au NPs are identical and obtained by the rotation of the initial. Interaction between 3 components is Van der Waals.

To resolve the interaction in the sensor, the time step was taken equal to 0.05 fsec with 32,768 steps (1.64 psec) for correlation evaluation at a few vibrational periods. It provides the frequency resolution of vibrational modes at $\Delta f = 20$ cm^{-1} and frequency interval length above 4000 cm^{-1} [42,43], which is comparable to the 15 cm^{-1} half-width of the Lorentzian function in the DFT calculation [48]. Collected single-bond spectra of nucleotides are orientation and conformation-dependent. The spectral resolution has been sufficient to the spectra's register structural, conformational, and interaction dependence.

There are two types of numerical noise in the MD spectra. One is from FFT itself; the other is the result of the projection of the velocity vector of the atom onto all bonds by which the atom has been connected to adjacent atoms, as shown in Figure 3a. The velocity autocorrelation function calculation for each bond has introduced low-intensity contributions of the adjacent bond into the calculated spectra. Therefore, only the highest peaks in

the spectrum are considered modes of the bond. The velocity vector contains the contribution of all interactions from adjacent bonds at each time step. The procedure of ring averages of the bond's spectra is shown in Figure 3b,c. The discrete spectral contributions of the atoms in the pyrimidine and purine rings were summed with equal unit weights to obtain nucleotide spectra of cytosine, thymine, adenine, and guanine. For cytosine and adenine, vibrational spectra for the methylated forms of nucleotides were also calculated. The summation of contributions from each bond is done in a single direction, either clockwise or counterclockwise, including each atom once and only into the single bond of the ring. The ring averages of the nucleotide spectra are introduced to compare them with the experimental Raman and SERS spectra. Averaging enhances modes distributed between adjacent bonds to an atom and cancels numerical noise in the spectra. That corresponds to measurement acquiring multiple spectra at time intervals summed up to enhance the modes. In MD, the correlation time steps and time interval relates to the accumulation of experimental spectra but the spectral map of each molecule bond can't be compared directly with the experiment. Therefore, proposed ring averages can evaluate cumulative vibrational spectra of oligomers comparable with experimental ones.

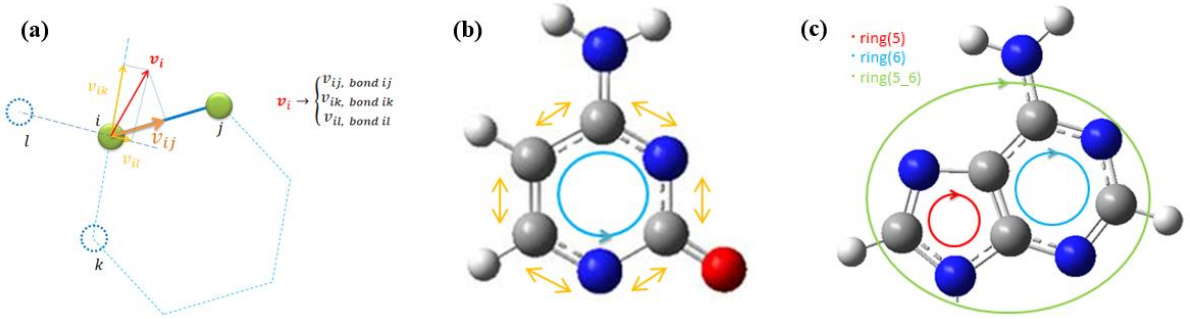

Figure 3. (**a**) The scheme of the velocity vector projection of the atom on the adjacent bond axes in autocorrelation function for each bond spectra, (**b**) the ring bond spectral averages in pyrimidine bases (averaged bonds are marked by yellow arrows, direction of bond summation is shown by blue circle with arrow), (**c**) the ring averages of purine bases with each atom spectra averaged only once in both pyrimidine (ring 6) and imidazole (ring 5) parts (direction of ring average is shown by blue and red circles, the bond connecting two rings is accounted for only once).

3. Results

In the current study, we estimated ring-averaged vibrational spectra for the four DNA nucleotides and the methylated forms of cytosine and adenine. Obtained spectra were compared to the results of the usual Raman measurement and the SERS experiments. The way to treat obtained MD vibrational spectra by machine learning random forest algorithm is also considered as related to the type of obtained data.

3.1. Ring Average Procedure for Puridine Type of Nucleotides

The ring average procedure has been tested for the adenine nucleotide first. The obtained by MD simulation averaged spectra are shown in Figure 4 for each of the pyrimidine and imidazole (rings 6 & 5) rings and for the combined rings. The averaged results were compared with the experimentally obtained Raman [50] spectra for DNA bases and SERS [51] spectra of single-stranded DNA fragments for the case of adenine; the high peak values of calculated spectra are compiled in Table 1 from Figure 4 together with data from the experiments [50,51]. The comparison of calculated frequencies with the experimentally measured ones with suggested attribution of vibrational modes from [50,51] is compiled in Table 1 for the frequency range up to 2000 cm^{-1}. Experimental measurements are done for nucleobases only in ref. [50], while ref. [51] represents SERS data for single-strand fragments measured in a different environment. The mode attribution is taken from the experimental data. The numbering of atoms in Table 1 is taken from ref. [50] (Figure 4 and

Table 1) with corresponding number of atoms referenced there reproduced in Table 1. The MD-calculated modes with frequencies close in value to measured ones are placed into the same table row. In the ring average, we could reproduce the stretching modes of the bond inside or attached to ring with relatively high accuracy at 997 cm^{-1}, 1119 cm^{-1}, 1323 cm^{-1}, and 1425 cm^{-1}. The ring breathing and stretching modes at 712 cm^{-1} and 1526 cm^{-1} were also reproduced within 30 cm^{-1} compared to the experimental results. Among bending and ring deformation modes with frequencies below 700 cm^{-1}, the 305 and 610 cm^{-1} bending modes are reproduced.

The ring averaging procedure leaves a large number of defined bending modes and reduces the number of well-defined stretching modes compared with the number of experimentally measured modes. These experimental frequencies not represented in the averages should be mostly attributed to the bond attached to the ring. Therefore, in addition to the ring averages, the bonds attached to the ring should be weighed and added to the whole spectra. The values of weight that could be utilized in averaging for the bonds attached to the ring are subject to study.

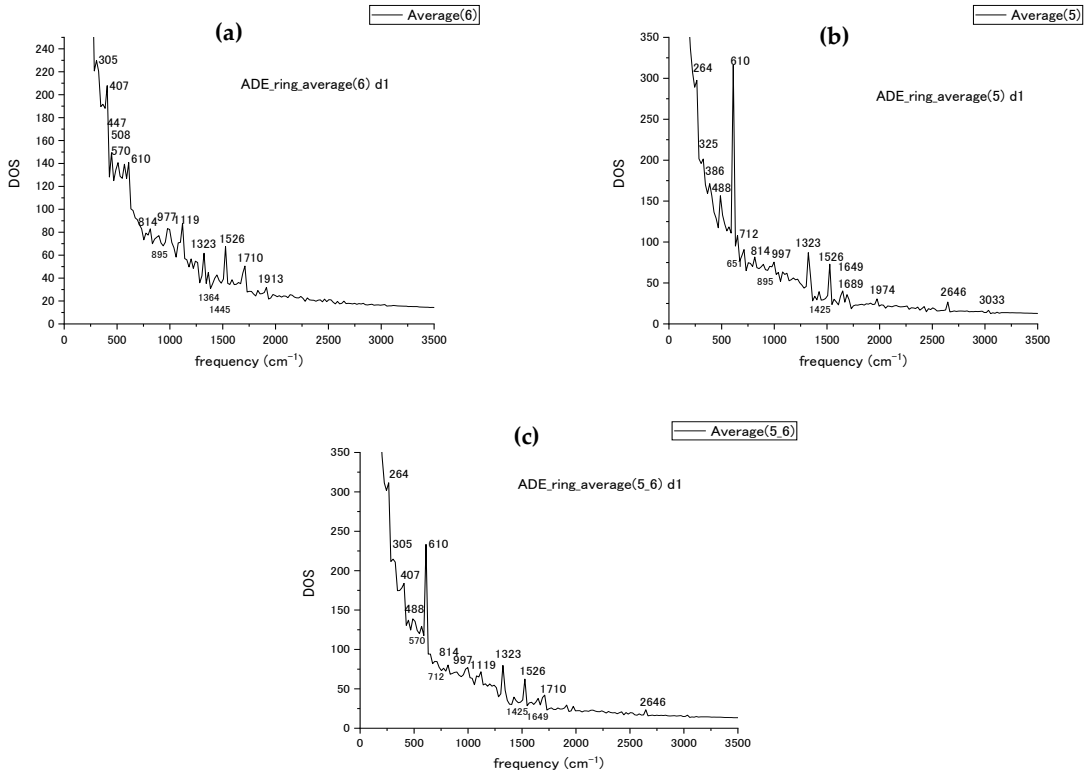

Figure 4. (**a**) The vibrational spectra of adenine pyrimidine ring (ring 6), (**b**) imidazole ring (ring 5), (**c**) the combined spectra for both rings of adenine with peak frequency values marked by numbers.

Table 1. Comparison of the experimentally available adenine Raman modes, ref.[50] and ref. [51], with our ring averaged results shown in Figure 4. The stretching and bending modes are indicated by letters (s) and (b). Attribution atom numbering is from the Figure 4 and Table 3 in ref. [50].

Experimental Bands, SERS, Adenine		**MD Calculated Vibrational Modes (~2000 cm^{-1}), Adenine**			**Assignments [50] (s)-Stretching, (b)-Bending**
1986 [50]	**2019 [51]**	**Average, Ring (6)**	**Average, Ring (5)**	**Average, Ring (6-5)**	
326		305	325	305	-C6N12(b)+N9R(b)
		407		407	
		447		447	

548		570		570	
626	628	610	610	610	N9R(b)+C6N12(b)-N7C5C6(b)
	684		651		
732	737		712	712	Ring stretching (breathing)
		814	814	814	
		895	895		
960	968	977	977	977	NH_2(r)+N1C6(s)
1028					
1122		1119	1119	1119	-N3C2(s)+N9R(s)
1194	1194				
1264	1270				
1334	1337	1323	1323	1323	-N7C5(s)+C8N7(s)
1370	1376	1364			
1390	1399				
1460	1455	1445	1425	1425	
1515	1550	1526	1526	1526	Ring stretching
		1710		1710	

3.2. Metylated Forms of Cytosine and Adenine

The vibrational spectra of the methylated forms of the cytosine and adenine nucleotides are subjected to the ring average procedure to understand the influence of the adjacent bonds on the unit weight of the ring bond in the average. The weights of each atom in ring bonds are kept unit for all three cytosine forms, Cytosine itself (CYT), 5-Methylcytosine (5MC), and 5-Hydroxymethylcytosine (HMC), for the vibrational spectra to be ring-averaged. T The result in Figure 5 includes the spectra for all three forms with our modes attribution [44] for cytosine in the left panel and a table of comparison of the MD calculated modes with the measured SERS frequencies [50,51] in the right panel. The comparison of MD with SERS modes of CYT [1] from ref. [50] and CYT [2] from ref. [51] for cytosine, given in the right panel of Figure 5, modes marked in color are present only in methylated forms of cytosine and have no corresponding experimental values that let us distinguish methylated forms by differences in spectra. The 203 and 285 cm^{-1} modes relate to ring deformation and the presence of N atoms in the ring. The 5-methyl and hydroxymethyl groups are attached to the C(3) atom of the ring as marked on the left pane, and the attachment will lead to changes in the stretching and bending modes in the 427, 692, and 1079 cm^{-1}. The amino group NH_2 causes changes in the 1750 cm^{-1} mode for HMC. It shows the possibility of spectral separation of the methylated forms by the presence or absence of indicating modes in cytosine vibrational spectra.

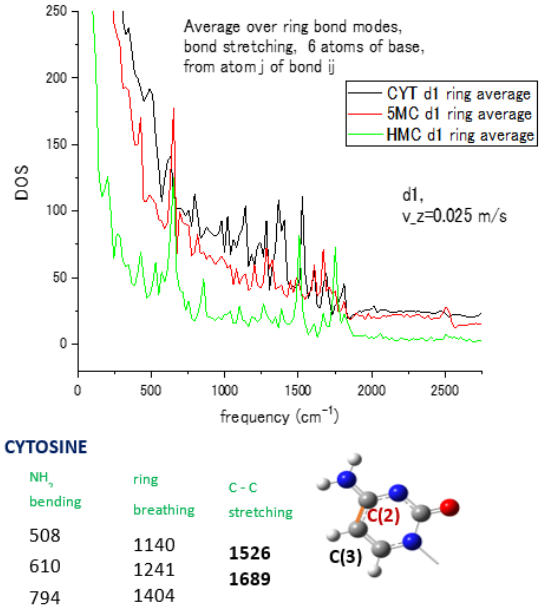

1986 SERS (CYT)[1]	2019 SERS (CYT)[2]	CYT	5MC	HMC
				203
				285
			427	427
470		488		529
616	600	631	651	651
			692	
		794	814	
	870	875		855
986		977	977	
1020	1041	1017		1038
			1079	1099
1140		1140	1140	
		1241	1201	
1306	1311	1282	1282	1262
1360		1364	1323	1343
1404	1423	1404	1445	1384
1526	1511	1526	1486	1506
1608		1608	1608	1608
		1689	1669	1669
				1750
		1811	1811	1811

Figure 5. Spectra and modes of cytosine (CYT) with methylated forms 5-Metylcytosine (5MC) and 5-Hydroxymethylcytosine (HMC): (Left pane) ring average of the spectra for 3 forms with mode attribution [44] of cytosine; (Right pane) comparison of MD and experimental SERS modes, with CYT [1] from ref. [50] and CYT [2] from ref. [51] for cytosine nucleotide, modes marked in color are present only in methylated forms of cytosine and have no corresponding experimental values.

3.3. Stability of the MD Vibrational Spectra vs.Interaction with 1 and 4 Au NP

To introduce multiple NP, we compared the influence of the number of Au NP (1 and 4 nanoparticles) on the spectra for cytosine and its methylated forms for nucleotides passing through the Au NP–graphene sensor. The different numbers of Au NPs influence the orientation and conformation of the nucleotides in the sensor during translocation and might influence interaction duration and strength. The graphs in Figure 6 compare the ring-averaged spectra of CYT, 5MC, and HMC in the case of 1 and 4 attached Au NPs. There was a similarity in the frequency or intensity of the peaks, with changes in some modes being revealed. A simple increase in the number of metal particles did not strongly increase the intensity of the peaks. Many of the peaks with increased intensity were vibration modes related to the O atom, methyl group CH_3, and amino group NH_2 attached to the pyrimidine ring. Interactions with the different numbers of Au NPs of ring-bonded groups lead to the relaxation of vibrational energy to other modes in the MD model. The attribution groups is shown for some high peaks in spectra for CYT, 5MC, and HMC in Figure 6. We can see a of spectral changes by largest contributions into the ring averages due to ring-bonded atoms and redistribution of mode intensities and possible slight mode shifts in 1100–1700 cm^{-1} interval that represents stretching modes in the ring and adjacent bonds. Therefore, instant values of modes will depend on the design of plasmon enhancer particles in such type of SERS sensor. The starting orientation of all three forms of cytosine nucleotide was kept the same. However, the presence of methyl and hydroxyl groups influenced the conformational motion of methylated forms during translocation, enhancing different frequency modes.

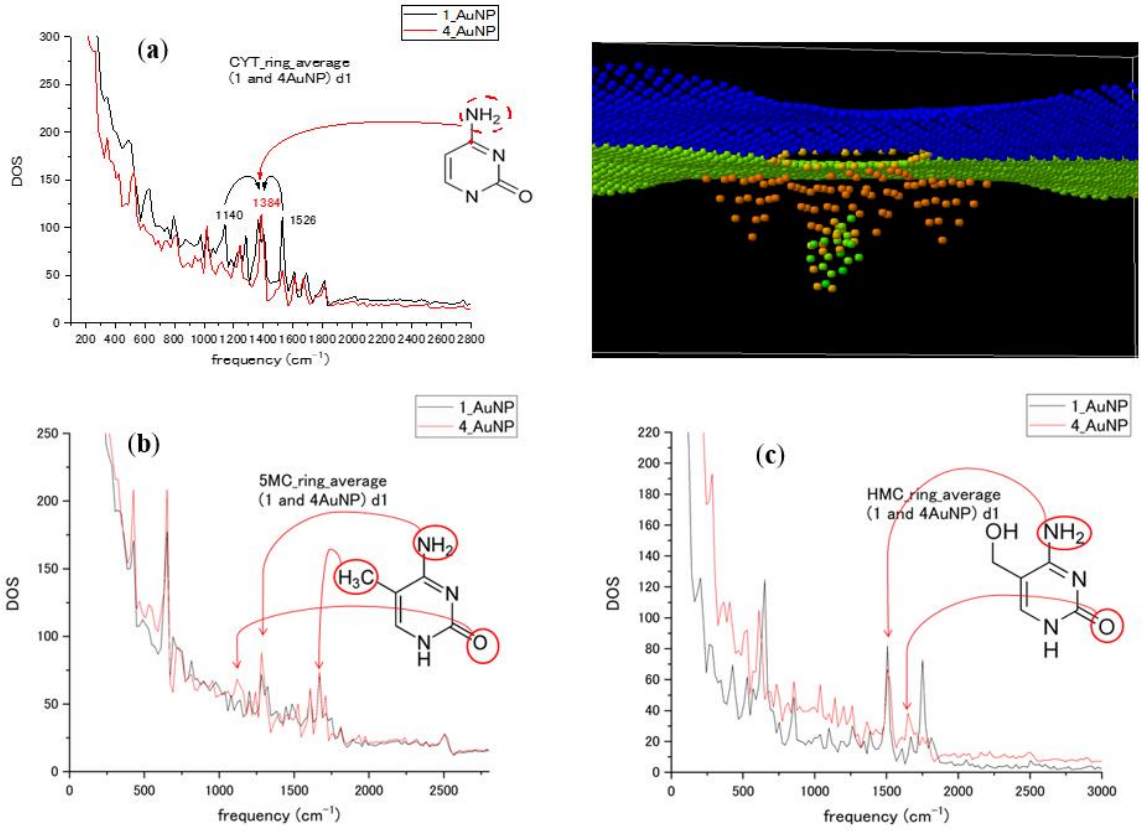

Figure 6. (**a**) Cytosine nucleotide ring average spectra calculated for 1 and 4 Au NPs attached to graphene nanopore (as shown in the upper right pane); (**b**) the corresponding spectra of 5-methylcytosine; (**c**) the spectra of 5-hydroxymethylcytosine. Attribution of some spectral peaks is shown for each form of cytosine.

3.4. Utilization of Machine Learning Algorithms for MD Spectra Recognition

The present SERS sampling includes accumulating a number of single-molecule spectra taken instantly at slightly changing orientation and conformation state, leading to the differences in measured spectra. Machine learning (ML)-assisted sampling of SERS substrates was implemented to improve data collection efficiency [52] in the experiment. ML algorithm was also applied to the ab initio calculation of Raman spectra of an ethylene molecule [41]. The spectra in the MD calculation are the results of Fourier transform of the velocity autocorrelation. We obtain the spectra at the same correlation interval for different interaction conditions and different modifications of nucleotides to be used as ML algorithm training sets. The applicability of the random forest algorithm was tested with the input of frequencies and intensities (F & I) of spectral peaks. The ring-averaged spectral data of cytosine and its methylated forms were used as the training set with the 80–20% test-train split of data. The test part was allocated either randomly (green line in (a, c, d)) or manually (violet line in (c & d)). The algorithm was taken from Python libraries. Figure 7 shows the MD calculated spectral data as blue, yellow, and red dots for CYT, 5MC, and HMC nucleotides in 1 Au NP case. The random forest prediction at the 2-parametric 86 points data set is shown as a green line in the (a) figure and gives a large error, especially above2000 cm^{-1}. To increase data set, the differences between nearest frequencies and intensities (ΔF and ΔI) were added into 4-parametric data set. The prediction error above 2000 cm^{-1} decreased, and the weights of the modes in the (F, I, ΔF, ΔI) data improved. Correspondence between the random and manual train-test split is tested in Figure 7c on the 4-parametric data set with converged prediction between splits below 700 cm^{-1} and sufficiently large difference above.

To double the size of the data set, we combined the data sets of vibrational spectra of 1 Au NP and 4 Au NP sensors for CYT, 5MC, and HMC nucleotides. The convergence interval of the prediction increased up to 1000 cm^{-1}. The error above 2000 cm^{-1} was also reduced, especially in a random split. Convergence between types of the split here indicates the spectral data set size sufficiency for prediction in the present 4-parametric representation. The spectra at different interaction conditions in the data set will improve the prediction power of the random forest algorithm as applied to the MD calculated vibrational spectra.

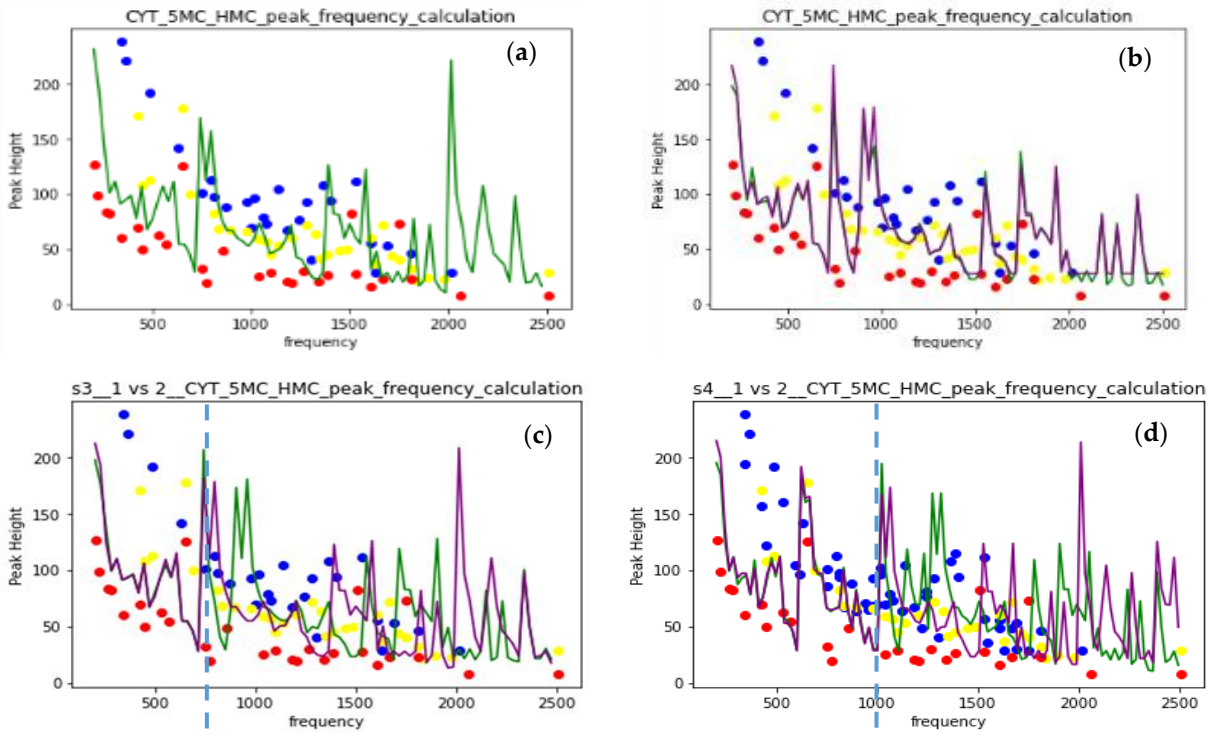

Figure 7. (**a**) Random forest prediction for 2-parametric (F & I) data set, random 0.2 split; (**b**) prediction for 4-parametric (F, I, ΔF, ΔI) data set, random 0.2 split (**c**) prediction for 4-parametric (F, I, ΔF, ΔI) data set, random and manual 0.2 split; (**d**) prediction for 4-parametric (F, I, ΔF, ΔI) data set, random and manual 0.2 split, data from 1 Au NP and 4 Au NP spectra.

4. Discussion

By averaging the spectra between ring bonds in nucleotides, we received oligomer vibrational spectra that reproduce the majority of modes obtained by Raman spectroscopy and SERS experiments with high accuracy. In cytosine, the methyl and hydroxyl groups are characterized by the following features: deformation vibrations of the entire ring bonds at 203 cm^{-1}, vibrations at the attachment of the deoxyribose to N atom at 285 cm^{-1}, stretching motion of the C- C atoms from 400 cm^{-1} to 1000 cm^{-1}, and oscillatory motion of the amino group attached to ring C atom at 1750 cm^{-1}. The change in the calculated sensor environment by the increase in the number of Au NPs resulted in a relaxation of the vibrational energy of oligomers due to the change in interaction. However, there was no significant mode change (variations in intensity and small frequency shifts) for standard and methylated forms of cytosine.

The possibility of applying machine learning algorithms to the prediction of MD calculated vibrational spectra has been investigated from the point of the training data set size and its parameter number. The use of spectra for the different interactions of the oligomer with the sensor environment as training data provides the required data set size to converge prediction. Such algorithm training on the calculated data can be used to predict

measured oligomer spectra in different single-molecule SERS sensors [53,54] with different types of plasmon enhancer structures.

Author Contributions: Conceptualization, methodology, software development, validation, supervision T.Z.; data curation and preparation, K.M.; writing—original draft preparation, review and editing, T.Z. All authors have read and agreed to the published version of the manuscript.

Funding: This research received no external funding.

Acknowledgments: T.Z. gratefully acknowledges the previous technical assistance in the calculations and preparation of the results on which current calculations were based done by Mohd Aidil Amin Bin Mohd Nasir and H. Yoshimizu. All calculations were performed at Applied Mechano-Informatics Laboratory in Toyama University.

Conflicts of Interest: The authors declare no conflict of interest.

References

1. Ardui, S.; Ameur, A.; Vermeesch, J.R.; Hestand, M.S. *Nucleic Acids Res*. **2018**, *46*, 2159–2168.
2. Ameur, A.; Kloosterman, W.P.; Hestand, M.S. *Trends Biotechnol*. **2019**, *37*, 72–85.
3. Han, X.X.; Rodriguez, R.S.; Haynes, C.L.; Ozaki, Y.; Zhao, B. *Nat. Rev. Methods Primers* **2022**, *1*, 87.
4. Stöckle, R.M.; Suh, Y.D.; Deckert, V.; Zenobi, R. *Chem. Phys. Lett.* **2000**, *318*, 131–136.
5. Hayazawa, N.; Inouye, Y.; Sekkat, Z.; Kawata, S. *Opt. Commun*. **2000**, *183*, 333–336.
6. Knoll, B.; Keilmann, F. *Nature* **1999**, *399*, 134–137.
7. Taubner, T.; Keilmann, F.; Hillenbrand, R. *Nano Lett.* **2004**, *4*, 1669–1672.
8. Zhu, Z.; Zhan, L.; Hou, C.; Wang, Z. *IEEE Photonics J.* **2012**, *4*, 1333–1339.
9. Anker, J.N.; Hall, W.P.; Lyandres, O.; Shah, N.C.; Zhao, J.; Van Duyne, R.P. *Nat. Mater*. **2008**, *7*, 442–453.
10. Saha, K.; Agasti, S.S.; Li, C.K.X.N.; Rotello, V.M. *Chem. Rev.* **2012**, *112*, 2739–2779.
11. Guerrini, L.; Krpetic, Z.; van Lierop, D.; Alvarez-Puebla, R.A.; Graham, D. *Angew. Chem. Int. Ed*. **2015**, *54*, 1144–1148.
12. Kneipp, K.; Wang, Y.; Kneipp, H.; Perelman, L.T.; Itzkan, I.; Dasari, R.R.; Field, M.S. *Phys. Rev. Lett*. **1997**, *78*, 1667–1670.
13. Greve, C.; Elsaesser, T. *Phys. Chem. B* **2013**, *117*, 14009–14017.
14. Garoli, D.; Haung, J.A. Ultrahigh sensitivity SERS detection of DNA and protein translocating through a plasmonic nanopores. In *Nanophotonics IX*; SPIE: 24 May 2022; Volume 12131, pp. 135–142.
15. Yang, J.M.; Jin, L.; Pan, Z.Q.; Zhou, Y.; Liu, H.L.; Ji, L.N.; Xia, X.H.; Wang, K. *Anal. Chem.* **2019**, *91*, 6275−6280.
16. Huang, J.; Mousavi, M.Z.; Giovannini, G.; Zhao, Y.; Hubarevich, A.; Soler, M.A.; Rocchia, W.; Garoli, D.; De Angelis, F. *Angew. Chem., Int. Ed*. **2020**, *59*, 11423−11431.
17. Huang, J.-A.; Mousavi, M.Z.; Zhao, Y.; Hubarevich, A.; Omeis, F.; Giovannini, G.; Schutte, M.; Garoli, D.; De Angelis, F. *Nat. Commun*. **2019**, *10*, 5321.
18. Xu, L.-J.; Lei, Z.-C.; Li, J.; Zong, C.; Yang, C.J.; Ren, B.J. *Am. Chem. Soc*. **2015**, *137*, 5149−5154.
19. Pazderka, T.; Kopecky, V. *Spectrochim. Acta Part A* **2017**, *185*, 207−216.
20. Wood; B. R.; Caspers; P.; Puppels; G. J.; Pandiancherri; S.; McNaughton, D. *Anal. Bioanal. Chem*. **2007**, *387*, 1691−1703.
21. Luo; X.; Xing; Y.; Galvan; D. D.; Zheng; E.; Wu; P.; Cai; C.; Yu, Q. *ACS Sensors* **2019**, *4*, 1534−1542.
22. Ren; W.; Damayanti; N. P.; Wang; X.; Irudayaraj, J.M.K. *Chem. Commun*. **2016**, *52*, 410−413.
23. Zhou; J.; Zhou; P.-L.; Shen; Q.; Ahmed; S. A.; Pan; X.-T.; Liu; H.-L.; Ding; X.-L.; Li; J.; Wang; K.; Xia, X.-H. *Anal. Chem.* **2021**, *93*, 11679−11685.
24. Doyle, F., Lapsia, S.; Spadaro, S.; Wurz, Z.E.; Bhaduri-McIntosh, S.; Tenenbaum, S.A. *Sci. Rep*. **2017**, *7*, 45393–45393.
25. Almehmadi, L.M.; Curley, S.M.; Tokranova, N.A.; N.A.; Tenenbaum, S.A.; Lednev, I.K. *Sci. Rep*. **2019**, *9*, 12356.
26. Li, J.; Gershow, M.; Golovchenko, J.A. *Nat. Mater.* **2003**, *2*, 611–615.
27. Yang, N.; Jiang, X. *Carbon* **2017**, *115*, 293–311.
28. Thompson, J.; Milos, P.M. *Genome Bio.* **2011**, *12*, 217.
29. Shankla, M.; Aksimentiev, A. *Nat. Commun*. **2014**, *5*, 5171.
30. Liang, L.; Shen, J.-W.; Zhang, Z.; Wang, Q.; *Biosens. Bioelectron.* **2017**, *89*, 280–292.
31. Zhang, Z.; Shen, J.-W.; Wang, H.; Wang, Q.; Zhang, J.; Liang, L.; Ågren, H.; Tu, Y.J. *Phys. Chem. Lett.* **2014**, *5*, 1602–1607.
32. Liang, L.; Zhang, Z.; Shen, J.; Zhe, K.; Wang, Q.; Wu, T.; Ågren, H.; Tu, Y. *RSC Adv.* **2014**, *4*, 50494–50502.
33. Zhou, Z.; Hu, Y.; Wang, H.; Xu, Z.; Wang, W.; Bai, X.; Shan, X.; Lu, X. *Sci. Rep.* **2013**, *3*, 3287.
34. de Souza, F.A.L.; Amorim, R.G.; Scopel, W.L.; Scheicher, R.H. *Nanoscale* **2017**, *9*, 2207–2212.
35. Zhang, L.; Wang, X.; *Nanomaterials* **2016**, *6*, 111.

36. Gilbert, S.M.; Dunn, G.; Azizi, A.; Pham, T.; Shevitski, B.; Dimitrov, E.; Liu, S.; Aloni, S.; Zettl, A. *Sci. Rep.* **2017**, *7*, 15096.
37. Lee, D.; Lee, S.; Seong, G.H.; Choo, J.; Lee, E.K.; Gweon, D.-G.; Lee, S. *App. Spectroscopy* **2006**, *60*, 322A.
38. Bell, S.E.J.; Sirimuthu, N.M.S. *J. Am. Chem. Soc.* **2006**, *128*, 15580–15581.
39. Madzharova, F.; Heiner, Z.; Gühlke, M.; Kneipp, J.J. *Phys. Chem. C* **2016**, *120*, 15415–15423.
40. Chen, C.; Li, Y.; Kerman, S.; Neutens, P.; Willems, K.; Cornelissen, S.; Lagae, L.; Stakenborg, T.; Van Dorpe, P. *Nat. Commun.* **2018**, *9*, 1733.
41. Hu, W.; Ye, S.; Zhang, Y.; Li, T.; Zhang, G.; Luo, Y.; Mukamel, S.; Jiang, J.J. *Phys. Lett*. **2019**, *10*, 6026–6031.
42. Zolotoukhina, T.; Yamada, M.; Iwakura, S. In Proceedings of the 1st International Electronic Conference on Biosensors (IECB 2020), 2 -17 November 2020; p. 035671.
43. Zolotoukhina, T.; Yamada, M.; Iwakura, S. *Biosensors* **2021**, *11*, 37.
44. Zolotoukhina, T., Mohd Aidil Amin Bin Mohd Nasir, H. Yoshimizu, In Proceedings of the 2st International Electronic Conference on Biosensors (IECB 2022), 2 -17 November 2022; p. 035671.
45. Shankla, M.; Aksimentiev, A. *ACS Appl. Mater. Interfaces* **2020**, *12*, 26624–26634.
46. Wanunu, M.; Sutin, J.; McNally, B.; Chow, A.; Meller, A. *Biophys J.* **2008**, *95*, 4716–4725.
47. Lewis, L.J.; Combe, N.; Barrat, J.-L. *Phys. Rev. B* **2000**, *61*, 16084.
48. Latorre, F.; Kupfer, S.; Bocklitz, T.; Kinzel, D.; Trautmann, S.; Grafe, S.; Deckert, V. *Nanoscale* **2016**, *8*, 10229–10239.
49. Mante, P.-A.; Belliard, L.; Perrin, B. *Nanophotonics* **2018**, *7*, 1759–1780.
50. Otto, C.; Van den Tweel, T.J.J.; de Mu, F.F.M.; Greve, J.J. *Raman Spectrosc.* **1986**, *17*, 289–298.
51. Pyrak, E.; Jaworska, A.; Kudelski, A. *Molecules* **2019**, *24*, 3921.
52. Rojalin, T.; Antonio, D.; Kulkarni, A.; Carney, R.P. *Mach. Appl. Spectrosc.* **2022**, 76, 485-495.
53. Wang, X.; Huang, S.; Shu, H.; Sen, Y.; Bin, R. *Nature Rev. Phys*. **2020**, *2*, 253–271.
54. Han, X.X.; Rodriguez, R.S.; Haynes, C.L.; Ozaki, Y.; Zhao, B. *Nat. Rev. Methods Prim.* **2021**, *1*, 87.